Size-dependent plasticity and activation parameters of lithographically-produced silicon micropillars

Ming Chen, Juri Wehrs, Alla Sologubenko, Jacques Rabier, Johann Michler, Jeffrey Wheeler

Materials and Design 189 (2020) 108506

Contents lists available at ScienceDirect

Materials and Design

journal homepage: www.elsevier.com/locate/matdes

Size-dependent plasticity and activation parameters of lithographically-produced silicon micropillars

Ming Chen [a], Juri Wehrs [b], Alla S. Sologubenko [a], Jacques Rabier [c], Johann Michler [b], Jeffrey M. Wheeler [a,*]

[a] Laboratory for Nanometallurgy, ETH Zurich, HCI G 503, Vladimir-Prelog-Weg 1-5/10, 8093 Zurich, Switzerland
[b] Empa, Swiss Federal Laboratories for Materials Science and Technology, Laboratory for Mechanics of Materials and Nanostructures, Feuerwerkerstrasse 39, Thun CH-3602, Switzerland
[c] Institut Pprime, CNRS, Université de Poitiers, F-86962 Futuroscope Chasseneuil, France

HIGHLIGHTS

- Lithographic Si pillars achieve near ideal strength, 60% stronger than FIB pillars.
- Activation parameters indicate kink-pair nucleation in Si at low temperatures.
- Si transitions from full to partial dislocations gradually from 150 to 300 °C.
- A modified analytical model is proposed for the size-dependent strength of Si.

GRAPHICAL ABSTRACT

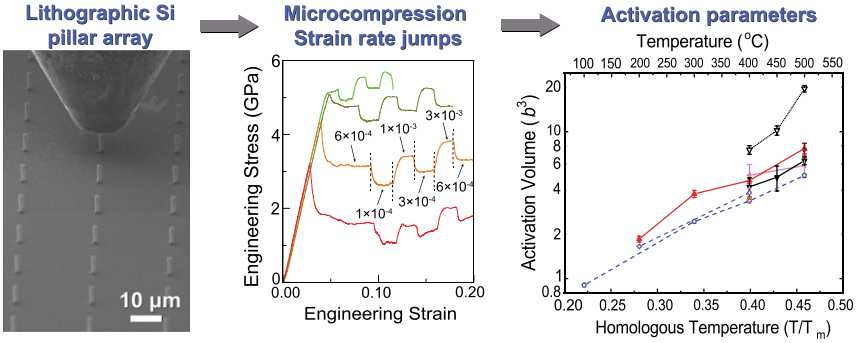

ARTICLE INFO

Article history:
Received 1 September 2019
Received in revised form 16 January 2020
Accepted 17 January 2020
Available online 21 January 2020

Keywords:
Silicon
Lithography
Plasticity
Activation parameters
Transient testing

ABSTRACT

Silicon is brittle at ambient temperature and pressure, but using micro-scale samples fabricated by focused ion beam (FIB) plasticity has been observed. However, typical drawbacks of this methodology are FIB-damage and surface amorphization. In this study, lithographic etching was employed to fabricate a large number of ⟨100⟩-oriented Si pillars with various diameters in the micro-scale. This allowed quantitative study of plasticity and the size effect of FIB-free Si in the brittle temperature range (25–500 °C) by conducting monotonic and transient microcompression in situ in the scanning electron microscope (SEM). Lithographic pillars achieved the ideal strength in temperature range of 25–100 °C and displayed significantly higher strengths (30–60%) than FIB-machined pillars because of the undamaged surface and the oxide layer confinement. The activation energy of deformation revealed a transition in dislocation mechanisms as a function of temperature. Strain rate sensitivity and activation volume measured from strain rate jump and stress relaxation tests indicated the surface nucleation of kink-pairs associated with the constricted dislocation motion in Si during deformation at temperatures below the brittle-ductile transition. A modified analytical model is proposed to accurately evaluate the size-dependent strength of covalent crystalline Si. The weak size effect observed in Si is attributed to the surface nucleation of dislocations and high lattice friction during their motion.

1. Introduction

Silicon is extensively used as a substrate or structural material for electronics devices, such as in microelectromechanical systems (MEMS), as

* Corresponding author.
E-mail address: jeff.wheeler@mat.ethz.ch (J.M. Wheeler).

https://doi.org/10.1016/j.matdes.2020.108506

well as the functional component in modern transistors at the micro- and nanometer scales. Recent advances in micromechanical testing techniques reveal that materials exhibit significantly enhanced strength and plasticity at small length scales, from microns to sub-microns, in contrast to conventional bulk behavior [1]. Thus, it is essential to understand the size effect on the mechanical properties and deformation behavior of Si for the reliable design of micro-scale structures and devices, as well for fundamental understanding of dislocation behavior in this important crystal structure.

Since the 1950s, extensive experimental and simulation work has been conducted to understand the dislocation-mediated plasticity in Si [2,3]. Diamond cubic-structured Si is considered to consist of two interpenetrating face-centered-cubic (fcc) lattices displaced by a/4 along the ⟨111⟩ direction [4]. This stacking of two closely packed atomic layers of each sublattice results in two sets of possible slip planes for dislocations [5]. At low temperatures, plastic deformation is governed by the glide of full dislocations on widely-spaced "shuffle" sets, and at elevated temperatures, it is dominated by the glide of Shockley partial dislocations on narrowly-spaced "glide" sets [6]. Si typically displays both high strength and intrinsic brittleness at ambient temperature due to the high lattice friction resulting from the strong covalent bonds. Previously, the fracture of Si was suppressed by either applying a confining pressure [7,8], or by testing specimens at elevated temperatures above the brittle-to-ductile transition (BDT) [9]. The latter approach only allowed the study of plastic deformation and dislocation mechanisms at high temperatures ($\geq 0.6T_m$) and omitted the regime of low and intermediate temperatures. Although the former method broadened the interrogated temperatures to a lower regime, the deviatoric stress modifies the dislocation core structure and affects the dislocation mechanism during deformation [10].

To study low temperature plasticity in Si, nanoindentation was initially used to investigate plastic deformation, since the confining pressure of indentation can suppress crack formation at ambient temperature. Si shows a phase transition from the diamond-cubic structure to the metallic β-Sn structure at pressures of ~12 GPa, due to the high hydrostatic confining pressure of the surrounding material [2,11]. However, dislocation-mediated plasticity was also observed beneath the indentation imprint due to the nucleation of dislocation at the free surface at room temperature [12]. Microcompression testing enabled the investigation of plasticity over a large temperature range without the complex strain state and high hydrostatic pressure during nanoindentation [13,14]. Preliminary microcompression results on Si revealed a strongly size-dependent brittle-ductile transition (BDT) at ambient temperature [15]. Further microcompression tests at elevated temperatures indicated that Si displays pronounced plasticity at temperatures between 200 and 500 °C ($\leq 0.45T_m$) [13]. Nevertheless, quantitative evaluation of plasticity and temperature-dependent dislocation mechanisms is still limited in this brittle temperature regime.

Furthermore, one of the major concerns of previous studies was the effect of FIB-damage on nanostructured Si during deformation. This issue has already been reported for various crystalline materials [16], where the ion irradiation and implantation of the sample surface significantly altered the mechanical properties of the miniaturized specimens. In Si samples, it has been shown that micropillars were stronger and less ductile after converting the FIB-induced amorphous layer to recrystallized Si at the surface through a thermal treatment [17]. FIB-free Si pillars fabricated by reactive ion etching also exhibited limited plasticity at relative low temperatures [14]. Thus, it is necessary to avoid FIB-damage in order to accurately assess the intrinsic mechanical properties of micro-scale Si.

In this study, an alternative process using lithography and reactive ion etching (RIE) was employed to fabricate Si micropillars with different diameters in the micron scale range. This provided a large array of FIB-free samples to be tested in the conventionally brittle temperature range of 25–500 °C. Moreover, since lithography and RIE techniques are widely used as microfabrication methods for semiconductors, the mechanical behavior of Si structures fabricated using this process is highly industrially relevant. In addition to monotonic compression at various temperatures and pillar diameters, transient plasticity tests were performed to extract activation parameters of the deformation mechanisms of Si by varying the temperatures. The resulting mechanical performance was compared to the FIB-machined samples, and the deformed microstructures were analyzed using scanning electron microscope (SEM) and transmission electron microscope (TEM). This allowed the correlation of the measured activation parameters to the deformed microstructural features and deformation mechanisms. The current work includes results from the testing of 220 micropillars to encompass a systematic investigation about the effect of size, temperature, strain rate and crystalline orientation on Si plasticity.

2. Experimental

2.1. Sample preparation and characterization

Arrays of pillars were fabricated by the Bosch process using ultraviolet (UV) lithography combined with reactive ion etching [18] on single crystal Si wafers (4 in. diameter, ⟨100⟩ orientation, P/B-doped, 525 μm thickness), as shown in Fig. 1a. Details of the lithography and RIE processes can be found in [19] and the supporting information. Cylindrical pillars were fabricated with diameters of 0.8, 1.7, 6.6 and 16.2 μm and with heights aimed to achieved an aspect ratio of ~3. The geometric details of the samples are listed in Table 1. After etching, a cap of SiO_2 layer was observed on the top of the pillar with smaller diameters, i.e., 0.8 and 1.7 μm, shown in Fig. 1b. The purpose of this additional oxidation layer was to protect the top surface of the smaller pillars from an undercut at the interface between the photoresist layer and the top of micropillar. For the larger pillars with diameters of 6.6 and 16.2 μm, a deep etching was performed by applying a pulsed room-temperature etch called the Bosch process, during which the etching process was switched back and forth between the etching using SF_6 lasting a few seconds and the sidewall passivating using C_4F_8 also lasting a few seconds [18]. The lithographic pillars exhibited a taper angle only around 2° at the root. The resulted strain and stress errors were about 1–2% in the negligible range according to previous finite element mothed simulation [20]. Since the diameter of pillars varies along the axis of the cylindrical pillar due to taper, a standard measurement close to the root of the pillar at 20% height (indicated in Fig. 1c) was applied to determine the pillar diameters. This is also the region where deformation was commonly observed to occur at elevated temperatures.

To compare the different specimen preparation techniques and crystalline orientations of the pillars, 2 μm diameter micropillars with an aspect ratio of ~3 were also produced on the ⟨100⟩-, ⟨111⟩- and ⟨123⟩-oriented Si wafers using a gallium (Ga^+) FIB station. This was performed using a Tescan Lyra (Tescan, Brno, Czech Republic) instrument operated at an acceleration voltage of 30 keV. Progressively smaller milling currents were employed in multiple stages to produce the pillars. An initial current of 9.3 nA was used for coarse milling, and then a smaller current of 0.79 nA was applied to obtain the pillar close to the designed geometry. A final polish was performed using an 80 pA current to minimize taper and achieve the final dimensions.

2.2. Micromechanical testing

After the pillar preparation process, micromechanical testing was performed on the Si pillars using an Alemnis indenter modified for high temperature operation *in situ* in a DSM 962 SEM (Carl Zeiss AG, Jena, Germany) operated at 5 keV [21]. Microcompression testing was performed from ambient temperature to 500 °C, which covers the Si homologous temperature (T/T_m) range of 0.18–0.46. To minimize thermal drift at the micrometer and submicron scales for each test temperature, both displacement drift and temperature shift measurements were conducted to achieve isothermal contact prior to testing [22]. Furthermore,

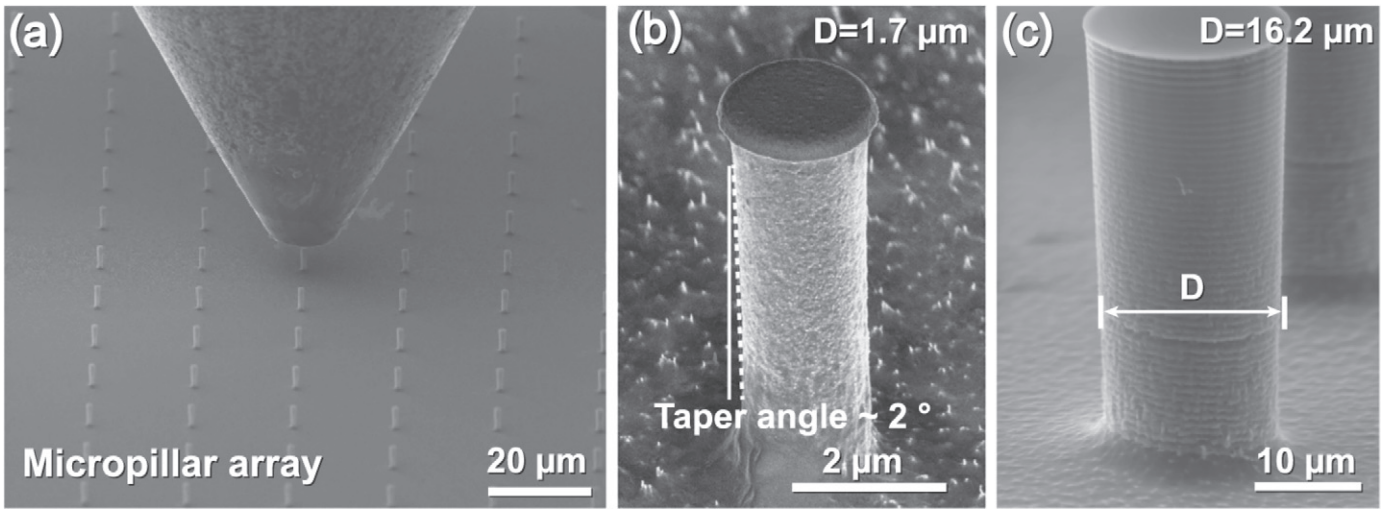

Fig. 1. Secondary electron (SE) micrographs of lithographic pillars before deformation: (a) pillar array, (b) 1.7 μm and (c) 16.2 μm diameter pillars.

a temperature-calibrated heated indenter tip was employed to accurately reference the exact testing temperature at the contact [23]. To remove the influence of any remaining thermal drift, a drift hold period of 60 s was performed at a constant low load during unloading of the samples to measure the thermal drift for each temperature, which was then subtracted from the measured data during the subsequent analysis [24].

Monotonic and transient tests were both employed to systematically study the micromechanical properties of Si. The yield strength and deformation behaviors were obtained via monotonic compression with a constant strain rate of 1×10^{-3} s^{-1}. When pillars showed sufficient plasticity, the strain rate sensitivity, m, and apparent activation volume, V_{app}, of the plastic deformation were determined by carrying out the transient tests, i.e., strain rate jumps (SRJ) and stress relaxation (SR), at elevated temperatures. The pattern of strain rates employed during the SRJ tests began with first compressing with a strain rate of 6×10^{-4} s^{-1} until achieving a steady flow regime that was observed as a plateau after the onset of yielding, then the strain rate was jumped to 1×10^{-4}, 1×10^{-3}, 3×10^{-4} and 3×10^{-3} s^{-1} sequentially at 2% strain increments for each jump before returning to the final strain rate of 6×10^{-4} s^{-1} (labelled in Fig. 3a, Supplementary material Video 1). There were some variations in the strains at which the strain rate jumps were performed for individual experiments at different temperatures, as depicted in the stress-strain curves. This was due to variation in the distance between the initial displacement of the indenter and the exact contact point of the indenter and micropillars in each experiment. Since displacement control was used in all cases, the contact point was determined after the tests. Stress relaxation (SR) tests were also performed to obtain the apparent activation volume, V_{app}, of plastic deformation in the 6.6 μm diameter Si micropillars at a constant strain at elevated temperatures. The pillar was loaded with a strain rate of 6×10^{-4} s^{-1} until 9% strain. At this point, a steady flow of the pillar was achieved, and a constant displacement was held for 5 min to relax the stress (shown in Supplementary material Video 2). After holding, the micropillar was reloaded until reaching 16% engineering strain.

Table 1
Geometries of pillars fabricated by lithography and reactive ion etching.

Diameter (μm)	Height (μm)	Aspect ratio (height/diameter)
0.8 ± 0.08	3.2	4.0
1.7 ± 0.1	4.8	2.8
6.6 ± 0.06	21.6	3.3
16.2 ± 0.11	46.0	2.8

2.3. Microstructure analyses

The surface morphology of pillars was imaged in a high resolution scanning electron microscope (Magellan, Thermo Scientific) operated at 3 keV. The study of defect structures was performed using a Talos F200X instrument (Thermo Scientific) operated at 200 keV in both transmission electron microscopy (TEM) and scanning TEM (STEM) modes and equipped with the SuperX energy dispersive X-ray spectrometry (EDS) module. EDS STEM was used for the elemental content analyses using a STEM probe size of about 0.7 nm and the probe current of about 70 pA. For the TEM analysis of the defect structures of the pristine and deformed lithographic pillars, FIB-lamellae were produced using a Helios G3 station (Thermo Scientific) operated at 30 keV of Ga^+ beam and 5 keV of electron beam sources. To minimize FIB-induced artefacts during the TEM lamella preparation, steadily reducing ion beam currents down to 7 pA were used for the final polishing of the lamella surfaces.

3. Results

3.1. Monotonic microcompression

The deformation behavior of lithographically-processed Si was observed to change significantly with temperature and sample size. Engineering stress-strain curves were measured during monotonic compression of Si pillars with different diameters, i.e., 0.8, 1.7, 6.6 and 16.2 μm, at various temperatures. In general, as the testing temperature increased, strength was observed to decrease while plasticity was enhanced in the Si pillars, as depicted in Fig. 2. At low temperatures, i.e., $T \leq 100$ °C, the Si pillars were brittle with no significant plastic strain especially at ambient temperature. In the intermediate temperature range of $100 \leq T \leq 300$ °C, limited plasticity was observed in the stress-strain curves as a short plateau after linear-elastic regime. In this temperature range, the plastic deformation is mediated by the slip of full dislocations on the {111} shuffle set planes along the ⟨110⟩-direction [2,15]. However, the mobility of full dislocation is still limited in Si, which has high lattice friction at this temperature range. In the larger 16.2 μm pillars, failure stresses did not notably decrease with increasing temperature below 300 °C. This is attributed to premature fracture in 16.2 μm pillars, which were quite brittle without visible plasticity below 200 °C according to the flow curves. Pillars catastrophically fractured due to crack formation during deformation at low temperatures.

When the temperature was increased to $400 < T < 500$ °C, Si pillars displayed pronounced plasticity. The stress-strain curves were characterized by an upper yield point with a stress drop, as shown in Fig. 2.

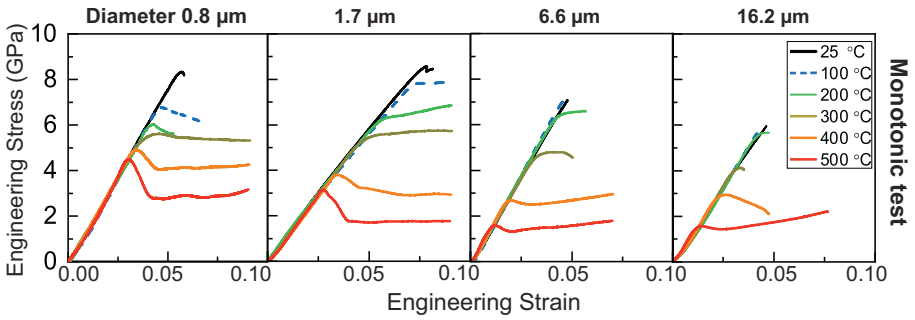

Fig. 2. Engineering stress-strain curves from monotonic microcompression testing with a constant strain rate of 1×10^{-3} s^{-1}.

This is in good agreement with previous experiments conducted in dislocation-free bulk Si [9], but it is contrary to the continuous yielding of the FIB-machined Si micropillars by Korte et al. [13,15]. The disparity in flow behavior between lithographic and FIB-machined pillars has also been observed in microcompression of GaAs [24]. This phenomenon revealed that dislocation-mediated plasticity in micro-scale semiconductors was significantly affected by microfabrication process. Moreover, the diameter of the micropillar is another crucial parameter that affects the mechanical properties of Si. Smaller pillars with diameters of 0.8 and 1.7 μm were more ductile and had an elongated plateau of steady flow compared to the large pillars with diameters of 6.6 and 16.2 μm at the same temperature.

3.2. Transient microcompression

Recently, transient plasticity testing techniques were developed and applied to nanoindentation and microcompression testing geometries [25]. Transient plasticity tests, i.e., strain rate jumps (SRJ) and stress relaxation (SR), were both employed to extract the strain rate sensitivity (SRS), m, and the apparent activation volume, V_{app}, of Si at conventionally brittle temperature range of 200–500 °C. These activation parameters allow the quantification of different deformation mechanisms in Si in the various temperature regimes. Moreover, the dynamic variation of the strain rate during a single compression test enables efficient and accurate access to strain rate-dependent deformation mechanisms with a reduced influence from the creep on the thermal drift by reducing the testing time. The deformed microstructure was kept more consistent within a single pillar during SRJ compression in contrast to multiple pillars being compressed at various strain rates using the monotonic compression [25,26].

As shown in Fig. 3a, SRJ microcompression was performed on Si pillars with various diameters. The strain rates are labelled for each jump deformation range during compression. Since smaller pillars were more ductile than the larger ones, the available temperature of the transient test was wider, e.g., in the range of 200–500 °C, for 1.7 μm pillars. SRJ testing was

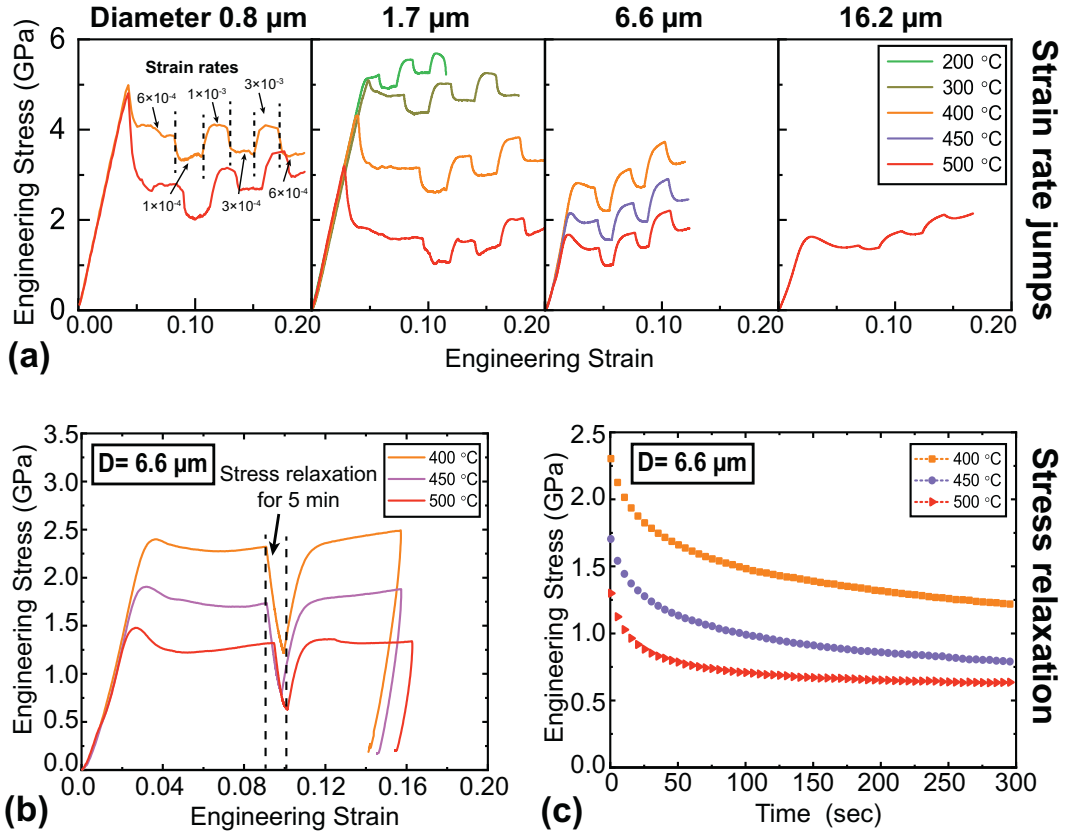

Fig. 3. Engineering stress-strain curves from microcompression with strain rate jumps of lithographic Si pillars with various diameters (a) and stress relaxation (b) of 6.6 μm diameter lithographic pillars in temperature range of 200–500 °C. (c) Logarithmic stress variation as a function of relaxation time during stress relaxation testing.

only conducted in the higher range of 400–500 °C for 6.6 and 16.2 μm pillars. A representative example is the 0.8 μm diameter pillar labelled with the corresponding strain rate to each jump (separated by dash lines). The stress-strain curves show that a constant flow stress plateau was reversibly achieved even after several jumps to different strain rates, during which the flow stress increased by jumping to a higher strain rate and remained relatively constant to achieve steady flow in each jump.

Flow stresses from each jump were averaged between several tests at the same temperature to determine the stress as a function of strain rate at each temperature [27]. Representative results from 1.7 μm diameter lithographic pillars are shown in the supplementary material Fig. S2. The flow curves and flow stress from the SRJ tests of FIB-machined pillars are displayed in Figs. S3 and S4. In all cases, the flow stress was observed to increase with increasing strain rate. The SRS, m, was calculated from the slope of this linear relationship on a log-log plot using the following equation [28]:

$$m = \frac{\partial \ln \sigma}{\partial \ln \dot{\varepsilon}}, \tag{1}$$

where m is the strain rate sensitivity exponent, σ is the flow stress and $\dot{\varepsilon}$ is the strain rate. The resulting values in Fig. 4a show that the SRS of lithographic and FIB-machined micropillars increased with the homologous temperature (T/T_m). Over the experimental temperature range, the SRS increases with homologous temperature from 0.02 to nearly 0.2, almost an order of magnitude increase, in pillars with various sizes and orientations. The slope of the SRS trend increases after 300 °C, revealing a transition in rate-limiting dislocation mechanism at higher temperatures [29].

The SRS, m, was then used to derive the V_{app}, which is related to the area swept by dislocation segments during a single thermally activated process at a constant temperature using the following equation [25,28]:

$$V_{app} = -\frac{\partial \Delta H(\tau)}{\partial \tau} = \frac{\sqrt{3} \cdot k_B \cdot T}{m \cdot \sigma}, \tag{2}$$

where $\Delta H(\tau)$ is the activation enthalpy of dislocation motion, k_B is the Boltzmann constant, and T is the absolute temperature in Kelvin. This value is usually scaled relative to the cube of the Burgers vector, b^3, to interpret different dislocation processes. Based on the previous compression tests by Korte et al. and pillar splitting tests by Lauener et al. of Si micropillars [13,30], full dislocations, $b = a/2\langle 110 \rangle$, were expected to be dominant at lower temperatures (< 150 °C), and Shockly partials, $b = a/6\langle 211 \rangle$, were considered to play a main role at higher temperatures (> 150 °C). Therefore, these values of the Burgers vectors were used to determine the V_{app} in the two temperature regimes, as plotted in Fig. 4b.

Stress relaxation (SR) testing was only conducted on 6.6 μm pillars at 400, 450 and 500 °C, as this diameter provided both sufficiently high loads and plasticity within the test temperature range to allow accurate measurements. According to results from SRJ testing in Fig. 4, the SRS and V_{app} have similar trends as a function of temperature in lithographic pillars with various diameters. Only the absolute values are slightly different, but they are within the same order of magnitude. The engineering stress-strain curves were shown in Fig. 3b. The flow stress of the pillar decreased with increasing temperature, but all flow curves exhibited full reversibility by achieving the same stress level before and after stress relaxation for 5 min. Some apparent straining occurred during stress relaxation due to the compliance of the load cell, since the load decreased with relaxing stress. However, the pillar remained at a relatively constant strain without additional deformation during relaxation according to *in situ* observation in the SEM. This compliance was corrected in flow curves during the post-mortem analysis. The flow curves from SR testing displayed a logarithmic decrease in stress as a function of relaxation time, as depicted in Fig. 3c. This is observed for many engineering materials and test conditions [28,31]. The relationship corresponds to the logarithmic equation [28]:

$$\Delta\tau = -\frac{k_B T}{V_{app(SR)}} \ln\left(1 + \frac{t}{c_r}\right), \tag{3}$$

where $\Delta\tau$ is the variation of shear stress during relaxation at a constant displacement, t is the relaxation time in second, and c_r is a time constant. By fitting a logarithmic function to the curves, $V_{app(SR)}$ is determined for each test temperature and then plotted in Fig. 4b. The activation volume from both transient tests manifested a similar tendency of V_{app} increasing with temperature. The V_{app} from SRJ tests on lithographic and FIB-machined pillars in all cases was very low, i.e., in the range of 1–8 b^3. However, the $V_{app(SR)}$ from SR tests was larger, i.e. in the range of 8–20 b^3, as twice as the values from SRJ tests. The underlying mechanisms for these values are discussed in relation to the deformed microstructures in the following sections.

3.3. Microstructure characterization

The deformed morphologies of the pillars are shown in Fig. 5 to illustrate the transition of deformation mechanisms as a function of temperatures. At lower temperatures, the pillars fractured at the base (Fig. S1a). Above 200 °C, the pillars were plastically deformed with slip lines (denoted by dotted lines) and sharp slip offsets at the sidewalls depicted in Fig. 5. The distance of slip offsets is at the range of hundreds of nanometers, e.g. about ~200 nm, showing in secondary electron (SE) micrographs (Fig. 5a). Such slip offsets resulted from collectively slip of about

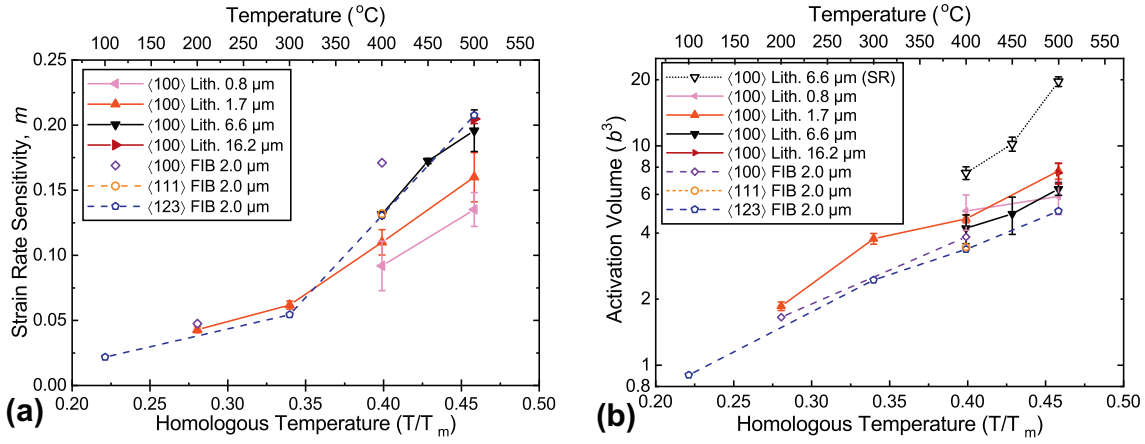

Fig. 4. (a) Strain rate sensitivity of lithographic pillars (solid symbols) with various diameters and FIB-machined pillars (hollow symbols) with various orientations as a function of homologous temperature (T/T_m). (b) Activation volume of Si calculated from SRJ and SR tests.

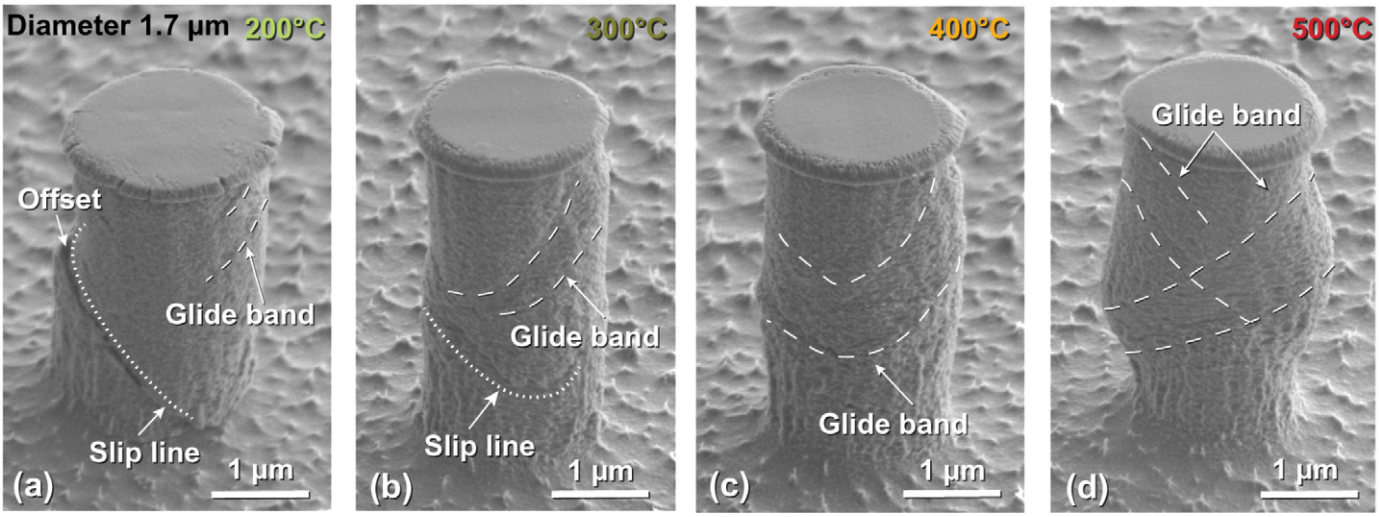

Fig. 5. Secondary electron (SE) micrographs of 1.7 μm diameter lithographic Si pillars after compression at (a) 200 °C, (b) 300 °C, (c) 400 °C and 500 °C.

500 full dislocations with an identical Burgers vector, $a/2\langle 110\rangle$ (length of $b = 0.38$ nm) [2], on the same {111} plane. In addition to the slip lines and offsets, glide bands also emerged at the side surface of the pillar, as marked by parallel dashed lines and arrows. These glide bands display a stack-of-cards morphology rather than a sharp offset. In diamond-cubic and zincblende structured semiconductors, the presence of these non-persistent glide bands is associated with extended multilayers of intrinsic stacking faults and/or twins [24]. This results from the glide of Shockley partial dislocations with a Burgers vector of $a/\sqrt{6}\langle 112\rangle$ on the {111} planes of Si. However, it is obvious that the slip offsets accommodated the majority of the plastic strain as compared to glide bands at 200 °C. As the temperature increased to 300 °C, glide bands extended to a larger fraction of the pillars and accommodated most of the pillar deformation, while slip lines became less pronounced with smaller offsets (Fig. 5b). With further increasing temperature, the micropillars were remarkably deformed, showing the intersection of broadened glide bands resulting from the activation of multiple slip systems (Fig. 5c and d). Thus, the partial dislocation mechanism is observed to co-exist with full dislocations after ~150 °C, and then becomes the dominant, rate-limiting mechanism after ~300 °C. The deformed microstructures were further investigated by transmission electron microscopy (TEM).

The pristine and deformed states of lithographic Si pillars were further characterized by producing FIB-lamella, and then observed in TEM and high resolution TEM (HRTEM) displayed in Figs. 6 and 7. The thin foil plane of lamella contained the ⟨100⟩ compression axis and the ⟨110⟩ slip direction. The bright-field (BF) image of the pristine pillar reveals a defect-scarce structure prior to deformation, as shown in Fig. 6a and b. The contrast in the micropillar derives from the curved surface of the bent lamella resulting in so-called bending contrast. This occurred because the lamella was quite thin, with a thickness in the range of 50–100 nm, but had a width and height of several microns. The EDX map of the upper part of the micropillar shows the SiO_2 cap from the thermal growth at the top surface of the pillar (Fig. 6c). Another thin layer of SiO_2 with a thickness of approximately 30–50 nm is observed at the sidewall of the pillar as a result of the etching process and natural oxidation.

Deformed structures were also examined using TEM to characterize the transition of dislocation mechanisms. At the transition temperature,

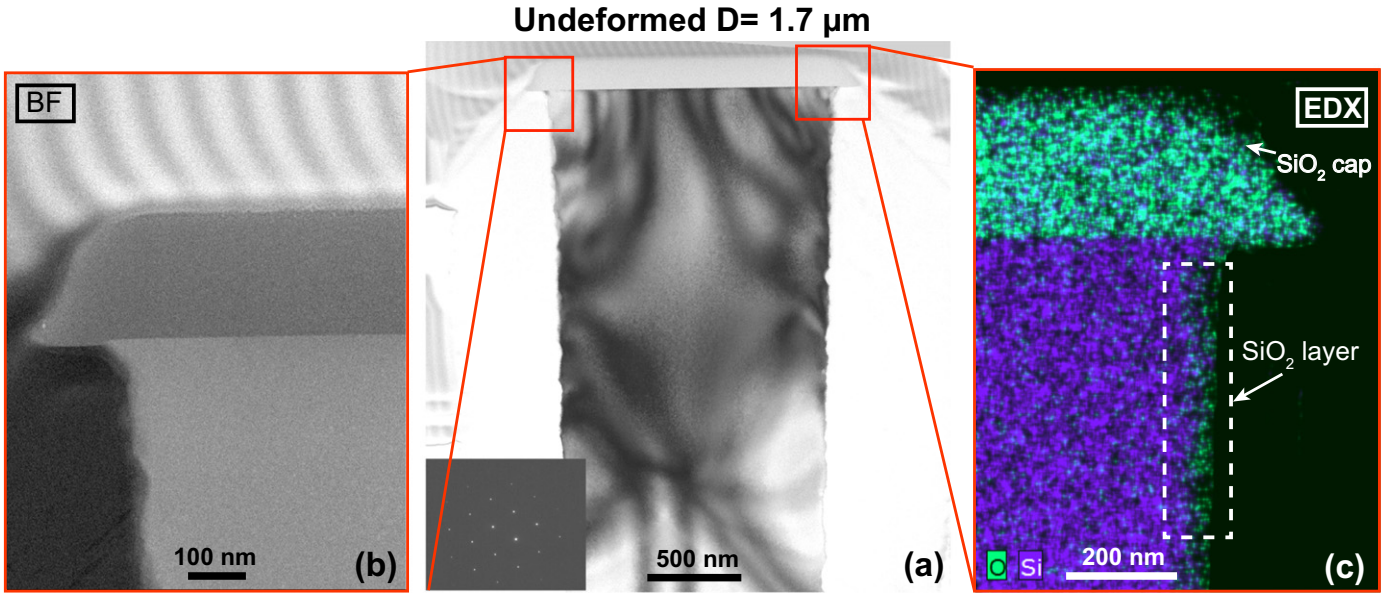

Fig. 6. TEM micrographs of pristine lithographic Si 1.7 μm pillar. (a) Bright-field (BF) image of a pillar before microcompression. (b) BF image of the sidewall of the pillar. (c) Corresponding EDX STEM elemental map of the top part of pillar.

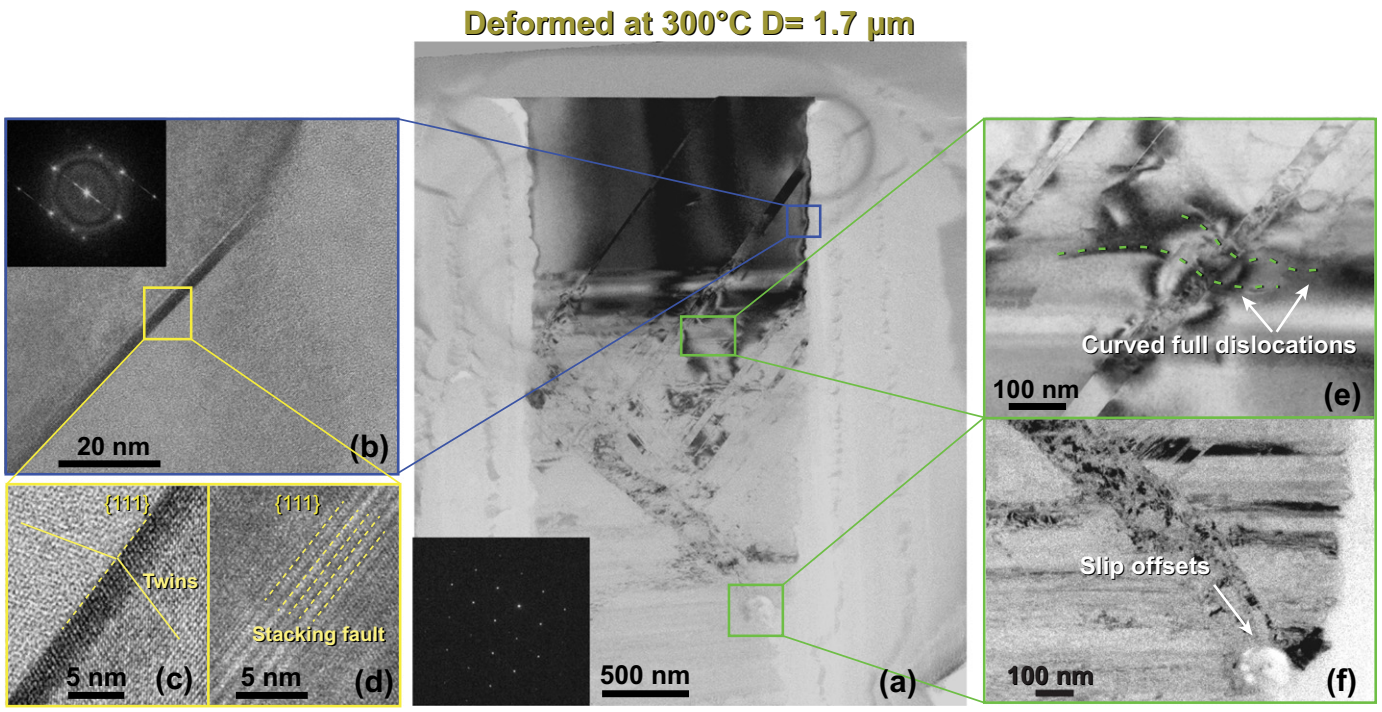

Fig. 7. TEM/HRTEM micrographs of a lithographic Si 1.7 μm pillar deformed at 300 °C. (a) BF image of a lamella cut from the deformed pillar. (b) Higher magnification of the slip band at the sidewall of the pillar. (c) High resolution micrograph of nanoscale twins and (d) stacking faults inside the slip band. (e) Magnified view of severe deformed regions containing large amounts of full dislocations. (f) Magnified view of slip offsets at the pillar surface.

300 °C, smaller pillars with 0.8 and 1.7 μm diameters displayed better plasticity without crack formation, in contrast to larger pillars with 6.6 and 16.2 μm diameters. A 1.7 μm lithographic pillar with a ⟨100⟩ orientation was chosen to investigate the deformation structures via post-mortem TEM characterization. This allowed direct comparison with the observations in FIB-machined, ⟨100⟩-oriented pillars by Korte et al. [13]. In the present, lithographic pillar compressed at 300 °C, a large number of defects were found to be distributed over the entire pillar (Fig. 7a). It was observed that the slip band manifested as a narrow band with a straight boundary with the undeformed matrix at the upper part of the pillar. These bands traversed across the entire width of the pillar and intersected with other deformed structures in the middle. The fast Fourier-transformed (FFT) diffraction pattern (Fig. 7b inset) of the glide band region exhibits a mixture of paired spots and elongated spots as well as the amorphous ring from the outside oxide, suggesting the co-existence of both nanotwins and stacking faults [2], which is consistent with the SEM observation of the deformed morphology in Fig. 5a. The direct evidence of this is confirmed by the high resolution lattice images in Fig. 7c and d. Since no internal dislocation-sources are observed in the pristine pillar (Fig. 6), these planar defects are suggested to result from the random nucleation of dislocations from the surface. Actually, this surface is the interface between crystalline core and oxide shell in the current lithography Si pillars. After that, dislocations were dissociated into Shockley partials during deformation. Thus, the defects were homogeneously distributed in whole pillars according to the contrast in TEM dark file (DF) image (Fig. 7a). This feature is entirely different with defects concentration at the top of FIB-machined Si pillars in TEM observation by Korte et al. [13].

In addition, limited full dislocations are also observed to interact with glide bands at 300 °C (Fig. 7e). During the interaction, the full dislocations were curved by shear of the lattice planes in the planar defects, i.e., nanotwins and stacking faults. As a consequence, the lattice distortion introduced by the curved full dislocations resulted in notable contrast within the deformation zone. Moreover, this deformation zone, which contained many full dislocations, terminated at the sidewall of the pillar, as the slip offset was also observed in the SEM (Fig. 5). In a previous TEM study of deformed Si pillars by Korte et al. [13], only limited plasticity featuring a few screw dislocations and cracks was observed after compression at ~100 °C, while a large amount of twins were observed after compression at 500 °C. By correlating these TEM results of deformation structures from various temperatures, it is shown that the deformation mechanisms in Si gradually transition from full dislocation controlled to partial dislocations dominating with increasing temperature.

4. Discussion

4.1. Activation energy of plastic deformation

4.1.1. Empirical method

Plasticity of Si micropillars was quantitatively analyzed by extracting the temperature-dependent activation energy, which in this case is the minimum energy that is needed for dislocation glide to overcome the Peierls barrier. The temperature dependence of Si strength was studied in the 1.7 μm diameter lithographic pillars by the monotonic compression. The critical resolved shear stress (CRSS), τ_{CRSS}, was calculated from the yield stress by applying the appropriate Schmid factor. This was 0.407 for the $a/2\langle 110\rangle\{111\}$ slip system of full dislocations (<150 °C) and 0.47 for the $a/6\langle 2\overline{11}\rangle\{111\}$ slip system of partials (>150 °C) with respect to the ⟨100⟩ force axis. For the {123} compression axis specimens at high temperatures, the Schmid factor was 0.471 for the partial dislocations. Fig. 8a shows the CRSS of 1.7 μm pillars with results from FIB-machined 2 μm pillars [13] and values from macroscale tests in literatures [8,9,19,32,33] for comparison. Over the entire temperature range, the τ_{CRSS} from compression of both lithographic and FIB-milled micropillars is one order of magnitude higher than the bulk counterparts due to the size effect [1,34]. Additional stress is necessary for dislocation nucleation at the early stage of plastic deformation in dislocation-free crystals at small scales due to the dislocation-source strengthening [35].

In previous semiconductor plasticity research, an empirical relationship of shear stress with reciprocal temperature was developed to

evaluate the activation energies, Q, of the individual dislocation mechanisms [2,26,36]:

$$\varepsilon = A(\tau_{CRSS})^{B}\ exp\left(-\frac{Q}{k_B T}\right), \tag{4}$$

where ε is the strain rate, A is a fitting parameter, τ_{CRSS} is the CRSS. The stress exponent B is in the range of 2–6 for dislocation-mediated plasticity at high stress but relatively low temperatures, i.e., homologous temperature (T/T_m) in range of 0.18–0.46 [37]. To glide on a slip plane, dislocations need to overcome an energy barrier by means of mechanical and thermal energy. The Q indicates the energy from thermal activation to move dislocations over one lattice unit during deformation at a finite temperature. The probability of sufficient activation energy, Q, occurring by thermal fluctuations to surpass this barrier at a finite temperature, T, is calculated by the Boltzmann factor, $\exp(-Q/k_B T)$. In this work, B is taken to be 3 to allow comparison with bulk testing of Si under the similar deformation temperatures and strain rates [38,39]. By taking the natural logarithm of Eq. (4), the correlation between τ_{CRSS} and T is expressed as follows:

$$\ln(\tau_{CRSS}) = \frac{1}{B}\ \ln\left(\frac{\varepsilon}{A}\right) + \frac{Q}{Bk_B}\cdot\frac{1}{T}, \tag{5}$$

Eq. (5) indicates a linear relationship between $\ln(\tau_{CRSS})$ and $1/T$ when ε is constant, and the Q can be extracted from the slope, as labelled in Fig. 8a. A change in slope on this Arrhenius plot indicates a transition of deformation mechanisms as a function of temperature, with different characteristic apparent activation energies Q/B. In Fig. 8a, both lithographic and FIB-milled micropillars exhibited consistent trends and similar activation energies with a transition appearing at ~300 °C. At this temperature, the deformation mechanism transitioned from a mixture of full and partial dislocations to partial dislocations being dominant at elevated temperatures. This is identical to the tendency of SRS and V_{app} (Fig. 4) from transient tests and is also supported by the deformed microstructure displayed in Fig. 5.

Moreover, the activation energy of full dislocation slip on the shuffle-set plane is smaller than partials glide on the glide-set plane. Thus, full dislocation mechanism is more energetically favored to be activated by stress at low temperatures where there is less thermal activation [15]. The Q from micropillar compression (~0.21 eV) at higher temperatures is comparable to the macroscopic tests by Castaing et al. under a confining pressure in the same temperature range [8], where the activation energy had values of 0.19 eV ($\varepsilon = 2\times10^{-5}\ s^{-1}$) and 0.26 eV ($\varepsilon = 2\times10^{-6}\ s^{-1}$). However, slight differences may be expected, since Castaing et al. conducted tests on samples with much higher dislocation densities due to pre-straining at high temperature. The results of bulk Si with a ⟨123⟩ orientation also showed larger values of Q at the higher temperature regimes. This disparity of activation energies may result from the much higher stress levels in micro-scale testing, since dislocation motion is stress-dependent in semiconductors [36]. Additional stress is necessary at small scales for dislocation

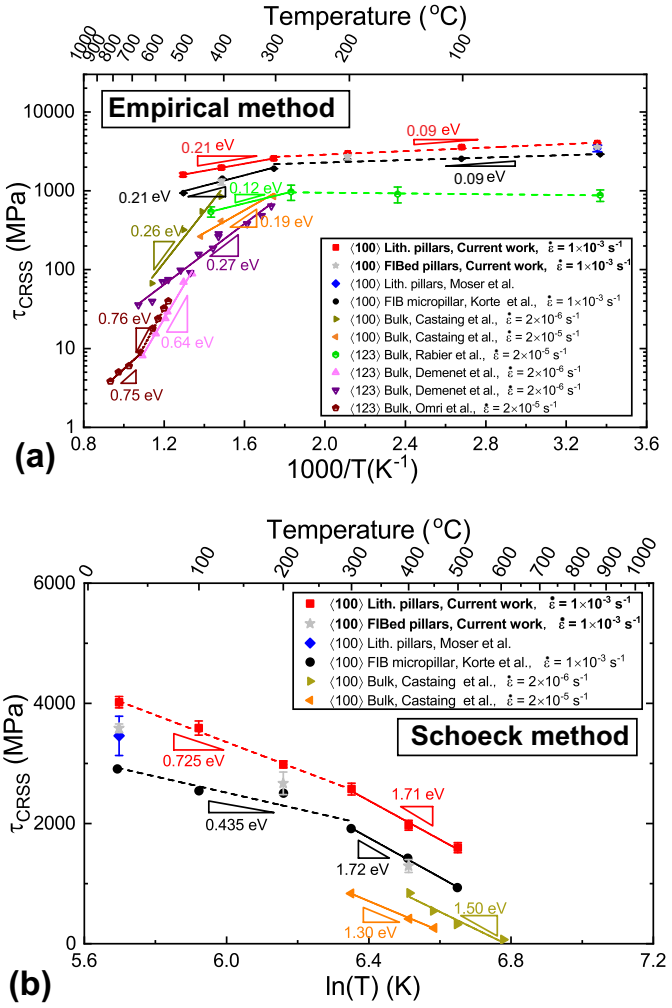

Fig. 8. (a) The critical resolved shear stress of 1.7 μm diameter pillars as a function of the reciprocal temperature from monotonic compression ($\varepsilon = 1\times10^{-3}\ s^{-1}$) using an empirical method and (b) as a function of the logarithmic temperature in the Schoeck method with apparent activation energies [8,9,13,19,32,33].

nucleation during deformation of micropillars compared to bulk testing of pre-strained Si with sufficient preexisting dislocations and/or sources.

4.1.2. Schoeck method

In the low temperature region (≤ 300 °C), the apparent activation energy was rather small, 0.09 eV, which means the dislocation motion was easily activated with a negligible energy barrier. Extrapolating to the lower temperature range, Q would be even approach zero. Therefore, Eq. (5) is no longer appropriate to describe the relationship of CRSS and T at high stresses and low temperatures with insufficient thermal activation for dislocation motion. Activation energy is more stress-dependent than temperature-dependent at the relatively low temperatures found in semiconductor compounds by Suzuki et al. [36], because the increased Peierls resistance in the covalently-bonded lattice strongly constricts the motion of dislocation. This constriction is even stronger in the compression of Si micropillars with measured stress levels one order of magnitude higher than in bulk samples. Thus, it is necessary to reconsider the activation energy in terms of stress-dependent dislocation motion using the rate equation below at low temperatures, as proposed by Schoeck et al. [40]:

$$\dot{\gamma} = \dot{\gamma}_0 e^{-\frac{\Delta H(\tau)}{k_B T}}, \tag{6}$$

then Q is equal to the activation enthalpy of dislocation motion:

$$Q = \Delta H(\tau) = -k_B T^2 \frac{\partial \ln \dot{\gamma}}{\partial T} = -T \cdot \left(k_B T \frac{\partial \ln \dot{\gamma}}{\partial \tau} \right) \cdot \frac{\partial \tau}{\partial T} = -T \cdot V_{app} \cdot \frac{\partial \tau}{\partial T}. \tag{7}$$

Solving for τ by integration of $\partial\tau$ and ∂T in Eq. (7), the linear relationship of CRSS with logarithmic temperature is described by the equation below:

$$\tau_{CRSS} = -\frac{Q}{V_{app}} lnT + c, \tag{8}$$

where V_{app} is the apparent activation volume at each temperature, and c is a fitting parameter. Q can then be extracted from the slope by applying the apparent activation volume, V_{app}, obtained from SRJ tests. To do this, the CRSS was replotted as a function of the logarithmic temperature in Fig. 8b. The slopes of the curves then show approximately the same values from both micropillar compression and bulk testing in the elevated temperature regime. Q is ~1.7 eV for the compression of micropillars, which is close to the values of 1.25 and 1.08 eV for bulk testing from Castaing et al. [8] by applying the same determined V_{app} from this study. Moreover, this result is also fairly close to the formation energy (1.4 eV) of kink-pair in Si in the same temperature condition [32,41]. This implies that the kink-pair nucleation process is activated once the energy overcomes the barrier of formation energy. Moreover, Q decreased to a smaller value of 0.725 eV for lithographic pillars and 0.435 eV for FIB-machined pillars at lower temperatures under high stress. This indicates the activation of dislocation motion is easier at low temperatures/high stresses. One possible reason for this is that the dislocation core is altered to a composite structure under high stress (~3–4 GPa) [42]. This composite core is likely to dissociate into glide-set and shuffle-set partials at low temperatures under high stress, rather than only glide-set partials observed at high temperatures [14,43]. Although the activation of dislocation motion is easier at low temperatures, the dislocation mobility is still restricted by the high lattice friction.

4.2. Strain rate sensitivity and apparent activation volume

To interpret the temperature-dependent dislocation activities in micro-scale Si, the strain rate sensitivity (SRS), m, and the apparent activation volume, V_{app}, were investigated in the conventionally brittle temperature range of 100–500 °C. This study also provided a direct comparison of plasticity data from two different transient tests at small scales. For the SRJ tests, lithographic pillars with various diameters and FIB-machined pillars with different crystalline orientations were tested to determine the influence of sample size and crystallographic orientation on plasticity in the temperature range of 100–500 °C. The increased SRS at elevated temperatures revealed that plastic deformation in Si is rate-limited at high temperature (Fig. 4a). The abrupt increase of the slope in SRS curves at 300 °C indicates the transition in deformation mechanism [26]. Based on the microstructural observations and activation energy calculation (Fig. 5 and Fig. 8), plastic deformation transitioned from a mixture of full and Shockley partial dislocations (< 300 °C) to purely partials dominating at higher temperatures (> 300 °C). Thus, the partial dislocation mechanism, i.e. formation of nanotwins and stacking faults, is a rate-controlling process in Si at elevated temperature. Moreover, larger micropillars displayed a higher SRS than smaller micropillars from lithography process. The SRS of FIB-machined 2 μm pillars with the ⟨100⟩, ⟨111⟩, and ⟨123⟩ orientations also increased with increasing temperature and displayed slightly larger values but on the same order of magnitude in contrast to the lithographic pillars. These SRS values were further applied to calculate the V_{app} to analyze the plasticity in different temperatures.

The values of V_{app} from SRJ tests in Si micropillars are quite small: 1–8 b^3. In macroscale tests, this magnitude of V_{app} usually suggests a deformation mechanism consisting of the nucleation and propagation of kink-pair dislocations from interfaces, such as grain boundaries in ultrafine-grained (UFG) metals (Ta and W) [44,45]. This limited activation volume is typical of kink-pairs, which form at low levels of thermal activation in high lattice friction materials where dislocation mobility is also limited [46]. The small V_{app} results from the confinement of dislocations due to closely-spaced obstacles from grain refinement and high defect density. In microscale tests, V_{app} is also quite small in single-crystalline (SC) refractory metals with high lattice friction, e.g. high entropy alloys and W [45,47]. This is attributed to the surface nucleation of kink-pair dislocations [48]. In the case of the present Si micropillars, the SC is grown by the Czochralski process which provides a defect-scarce structure (dislocation density below 10^8 m^{-2}) [39]. Thus, the small V_{app} is attributed to the influence of the high lattice friction on dislocation propagation, after surface nucleation, during deformation at low temperatures with limited thermal activation (Fig. 7a). Because the Peierls stress is fairly high in covalently-bonded Si (~ 3.8–4.5 GPa) [49], Si is considered to be analogous to refractory high entropy alloy and bcc W. Moreover, the lattice friction is further enhanced in the covalently-bonded lattice, since the reconstruction of dangling bonds broken by dislocation motion increases the Peierls potential [28,50]. The V_{app} slightly increased with increasing temperature, since the thermally-activated motion of the dislocations was enhanced. Moreover, the curves also indicate that the V_{app} is mostly independent of pillar diameter in lithographic pillars and of crystalline orientation in FIB-machined pillars, as they had nearly the same values at identical temperatures.

Furthermore, the V_{app} measured from SR tests (10–20 b^3) is twice as large as results from SRJ tests (Fig. 4b). This means the V_{app} was also affected by the experimental boundary conditions [51], by which different deformation rates were found to influence the dislocation movement during deformation. In SRJ testing, the strain rate was abruptly switched between various magnitude values, some of which were much larger than the strain rate in SR tests. This induces an overall higher deformation rate in SRJ testing. So sufficient dislocations were required to nucleate from the free surface in limited time, and then interact with other dislocations from the secondary slip system resulting in higher strain hardening in SRJ tests (Fig. 3a). While the previously nucleated dislocations can continuously glide to larger distances, inducing larger activation volumes during the 5 min of stress relaxation, in the SR tests.

4.3. Size-dependent strength

In addition to temperature and strain rate, the strength of Si is also dependent on the pillar diameter as shown in Fig. 9a. The τ_{CRSS} for the lithographic Si pillars with diameters of 1.7 μm at temperatures ≤100 °C achieved shear strengths (~4 GPa) that reach a large fraction of the shear modulus of Si, close to 6.69 GPa (G/10) [52] and to density functional theory predictions of ~6.8 GPa [53]. This level of τ_{CRSS} is close to the stress level for dislocation nucleation. This early stage plasticity is attributed to the nucleation and propagation of kink-pair dislocations from pillar surface during deformation. The strength of lithographic Si measured here is among the highest ever measured in micromechanical tests with comparable sample sizes [7,17]. As the pillar diameter increased, the strengthening effect is gradually reduced from these theoretical limits. The size effect on the flow strength of materials is empirically quantified in terms of a power-law relation [54], $\tau = C \cdot D^n$, where τ is critical resolved shear stress (CRSS), C is a fitting parameter, D is the size of sample, and the absolute value of n is called the size effect exponent to dictate the dependence of strength on the sample size. The CRSS was calculated by applying the appropriate Schmid factors, i.e., 0.407 for low temperatures ($T < 150$ °C) and 0.47 for high temperatures ($T > 150$ °C), according to the aforementioned transition of dislocation mechanism. Stress values of 0.8 μm diameter pillars were ignored in this fitting, since they significantly deviated from the power-law trend due to the buckling of several specimens during compression. This buckling behavior was induced by the large aspect ratio ~4 of 0.8 μm pillars (Table 1). The results in Fig. 9a demonstrate a weak size effect in Si, as the absolute values of n are in the range of 0.05–0.15 at temperatures below 300 °C. With increasing temperature, n increases to 0.46 at the 500 °C. This is similar to the results of MgO (n = 0.1–0.4) [22] and GaAs (n = 0.08–0.12) [55] in the same homologous temperature (T/T_m) range of 0.15–0.45, but it is still lower than bcc metals such as W and Ta (n = 0.3–0.8) [56] and fcc metals like Cu (n = 0.52–0.7) [57]. This indicates the size effect of covalent crystalline Si is similar to ionic crystals, but it is much weaker than metals.

The size effect is effectively governed by the lattice friction, dislocation density, and dislocation single-arm source lengths [35,58]. In metallic pillars with micrometer sizes, the dislocations are nucleated at sources inside micropillars and then pinned by the preexisted dislocations during gliding. Thus, the source strengthening is significantly affected by the dislocation density, which is in the moderate range of 10^{12}–10^{13} m^{-2} for metals [35,58]. Nevertheless, the size effect is effectively suppressed, when the metallic specimens are scaled down below 100 nm [48,59], because surface nucleation becomes the dominant mechanism due to insufficient internal sources. Dislocation nucleation is more energetically favorable at the surface, since atomic surface steps and defects facilitate the nucleation process [60]. However, in Si micropillars, the length scale for such surface nucleation dominated behavior is observed to increase to the micrometer scale. The reason for this is that the internal sources are already effectively depleted in microscale Si pillars due to the significantly lower dislocation density (~10^8 m^{-2}) compared to metals. Moreover, the smaller size effect in Si is also attributed to the high lattice friction, since the lattice resistance of covalent crystals is one or two orders of magnitude higher than metals [58]. The mobility of dislocations is considerably hindered by lattice friction, especially at low temperatures.

However, the power-law fitting of size-dependent strength still shows deviations at several data points in Fig. 9a. To precisely investigate the size effect in covalently bonded Si, a modified analytical

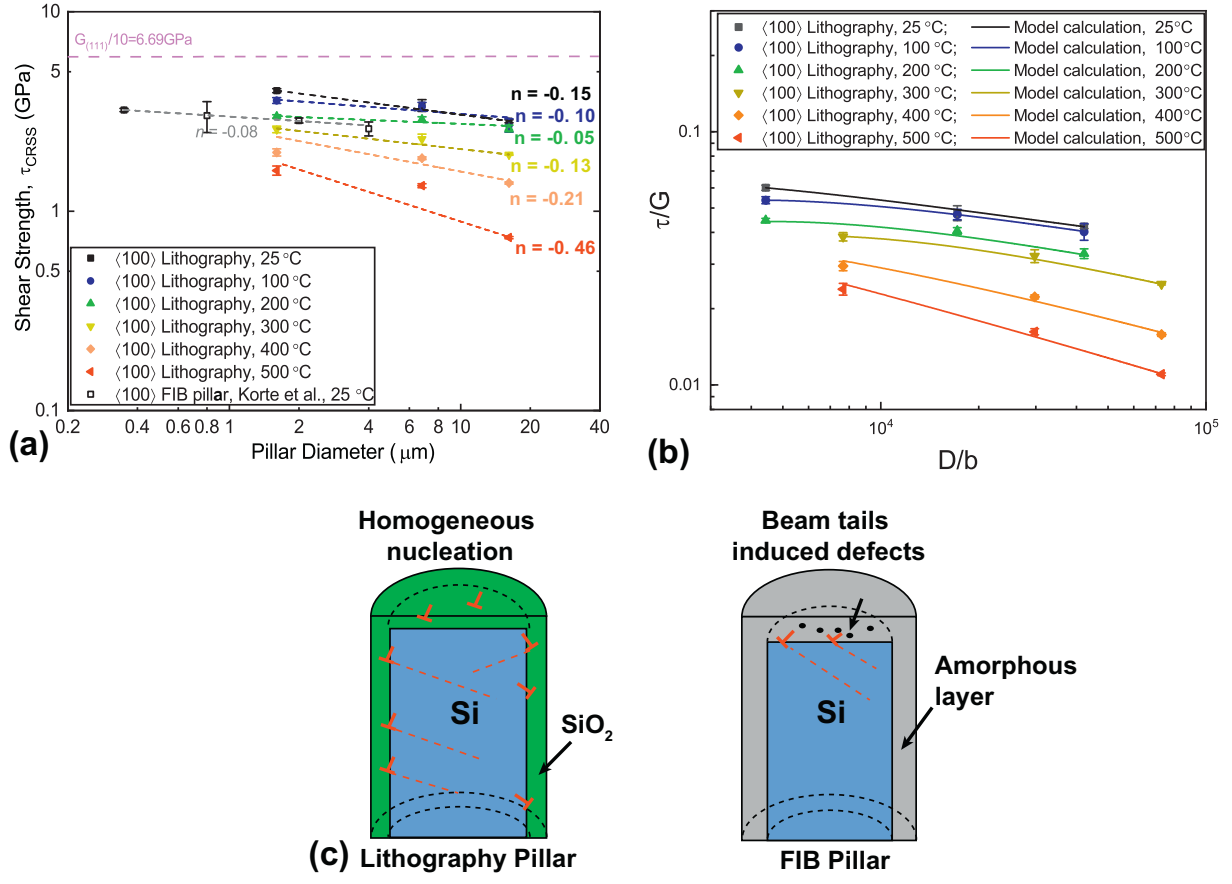

Fig. 9. (a) Critical resolved shear stress (CRSS) as a function of pillar diameter from monotonic compression ($\dot{\varepsilon} = 1 \times 10^{-3}$ s^{-1}) at various temperatures with comparison to literature values [13]. Dash curves were fitted by power-law relation. (b) Normalized strength was calculated as a function of normalized size (solid curves) for each temperature according to the analytical model (Eq. (14)). (c) Schematic of dislocation nucleation sites at the interface of lithography pillar and top interface of FIB-milled pillar.

model is proposed with the consideration of the contributions from different strengthening mechanisms. The CRSS of crystalline micro-scale materials can be described as the sum of the lattice friction τ_0, Taylor strengthening τ_G, and source strengthening τ_s expressed as [35,58]:

$$\tau_{CRSS} = \tau_0 + \tau_G + \tau_s. \tag{9}$$

In Eq. (9), τ_0 is the temperature-dependent stress for dislocation motion to overcome the Peierls potential of crystal lattice [61]:

$$\tau_0 = \begin{cases} \left[1-\left(\frac{T}{T_C}\right)^{0.5}\right]\tau_p, & T<T_C \\ 0, & T\geq T_C \end{cases}, \tag{10}$$

where τ_p is the Peierls stress (≈4.48 GPa) [49] at 0 K, T is testing temperature and T_C is the critical temperature for partial dislocation motion. The glide of full dislocations on the shuffle set is restricted by the high lattice friction below T_C, whereas the movement of partials on the glide set is promoted to become rate-limiting by sufficient thermal activation above T_C in covalent crystals [36]. The T_C is about 300 °C in Si according to the calculation of activation parameters (Figs. 4a and 5). The Taylor hardening, τ_G, in Eq. (9) is attributed to the pinning of mobile dislocations by the forest dislocations, and then expressed as:

$$\tau_G = \alpha b G\sqrt{\rho}, \tag{11}$$

where α is the a constant about 0.5, b is the Burgers vector of corresponding dislocation, G is the shear modulus of Si, 66.9 GPa [52], ρ is the dislocation density of Si in the order of ~10^8 m^{-2} [39].

The source strengthening, τ_s, indicates the minimum stress required to operate the single-arm sources in micropillars. It is commonly expressed as Eq. (12) according to three-dimensional discrete dislocation dynamics simulations [62]:

$$\tau_s = KG\frac{\ln(\overline{\lambda}/b)}{\overline{\lambda}/b}, \tag{12}$$

where K is a constant on the order of 0.1 and $\overline{\lambda}/b$ is the statistical average source length normalized by the Burgers vector b. The $\overline{\lambda}/b$ is commonly considered to be proportional to pillar diameter, D, divided by N, the natural number of dislocation sources (i.e. D/N), in metals with a strong size effect at micrometer scales [62]. The N is affected by the dislocation density and their distribution inside the pillar and at the surface. However, this is not the case in dislocation-scarce Si micropillars due to surface nucleation. Thus, we reconsider the relationship between the source length and pillar diameter by adding the exponent, m, to scale the contribution of normalized size versus dislocation source availability:

$$\overline{\lambda}/b = (D/bN)^m. \tag{13}$$

By merging Eqs. (10)–(13) into Eq. (9), the model for the size-dependent strength of covalently bonded Si is expressed as:

$$\frac{\tau_{CRSS}}{G} = \left[1-\left(\frac{T}{T_C}\right)^{0.5}\right]\frac{\tau_p}{G} + \alpha b\sqrt{\rho} + K\frac{\ln\left[(D/bN)^m\right]}{(D/bN)^m}. \tag{14}$$

As shown in Fig. 9b, the calculated values (solid curves), which take into account the change in b in the different temperature regimes, display good agreement to the experimental data with $m = 0.5$ and $N =$ 225–625 at all testing temperatures. This model reveals that the strengthening of Si micropillars can be mainly attributed to the Peierls stress and source strengthening, whereas the dislocation-related Taylor hardening ($\alpha b\sqrt{\rho} = 1\times10^{-6}$) is negligible in the dislocation-scarce Si.

4.4. Lithography etching versus FIB milling

The surface of Si micropillars plays a critical role as the dislocation nucleation sites during deformation. Thus, the plasticity in micro-scale covalent crystals is profoundly affected by the microfabrication process, because different surface states are achieved after specimen fabrication. The mechanical tests show the lithographic micropillars displayed a 30–60% greater strength than the FIB-machined pillars at each temperature (Fig. 8), which is consistent with findings for molybdenum and covalent GaAs [24,63]. The TEM observation on the FIB-machined Si pillar from Korte et al. [13] clearly shows that most of the cracks and deformation bands were located at the top of the micropillar with an amorphous shell, where defects originated from the top surface and then propagated into the body of the pillars (Fig. 9c). Even through the top surface of pillars was slightly exposed to Ga^+ irradiation due to beam tails, the defects were extensively implanted on the top surface with 90 deg. incidence angle. These defects promote the nucleation of dislocations and decrease the flow stress during the subsequent deformation.

Compared with FIB-milled pillars, the lithographic Si displays a different appearance with the defects more homogeneously distributed over the entire pillar after deformation, shown in Fig. 7a. Actually, lithographic etching induces an oxide layer with a thickness of 30–50 nm (in Fig. 6c) to passivate the side surface of pillars. This passivated oxide layer strengthens the pillars by suppressing the interface nucleation of dislocations and pinning mobile dislocations at the interface between the passivated layer and the inner surface of the pillar, as observed in metallic nanopillars and nanowires coated with oxides [59,64]. The dislocations then pile up and generate a back-stress to impede the further operation of the dislocation source at the interface. Moreover, the sidewall and body of the pristine pillar are almost free of defects, as indicated by the uniform contrast in the TEM BF image shown in Fig. 6a. The defect-depleted structure requires additional stress for dislocation nucleation from surface [65]. This surface nucleation mechanism was also observed to effectively increase the stress to theoretical strength and suppress the size effect in FIB-free Mo fibers from the matrix etching process [66]. Hence, the superior strength of the lithographic Si pillar resulted from the undamaged structure and the interfacial confinement of the passivated layer. UV lithography combined with reactive ion etching demonstrates a feasible method to prepare undamaged micro- and nanoscale samples for assessing intrinsic properties of materials and provides industrially-relevant data for microdevices. Further work is needed to deconvolute the effect of the confining passivation layer on the intrinsic size effect of Si.

5. Summary and conclusions

Plasticity of single crystalline Si as a function of temperature and pillar diameter was systematically investigated via microcompression of Si pillars fabricated by UV lithography combined with reactive ion etching and also by FIB milling. Lithographic pillars with small diameters achieved shear strengths of ~4 GPa, which approach the theoretical strength. This is 30–60% stronger than pillars with identical geometry from FIB milling. The superior strength of lithographic pillars is attributed to the relatively defect-free crystalline structure and the surface confinement of the oxide shell from the Bosch process.

The activation energy of the dislocation mechanisms was determined by considering two aspects: stress-dependent motion at low temperatures and mobility at high temperatures. The results indicate a shuffle-to-glide transition as the deformation mechanism changes from a full dislocation to partial dislocation dominant that emerged at ~300 °C. The change was confirmed by the appearance of stacking faults and nanotwins in TEM micrographs. Transient plasticity tests enabled the rate dependence of the plastic behavior to be quantitatively assessed in the conventionally brittle temperature range of 200–500 °C in Si. Pillars with various diameters displayed an identical tendency where the strain rate sensitivity increased at elevated temperatures, while the

partial dislocation mechanism is the rate-controlling process during deformation. The activation volume of lithographic and FIB-machined pillars was in the range of 1–8 b^3, indicating that the mechanisms of kink-pair nucleation from the pillar surface and the interaction between dislocations were the rate-limiting process.

A weak size effect, as compared to fcc and bcc metals, was observed in covalent Si, which is similar to ionic crystals. This is attributed to the surface nucleation mechanism and the high lattice resistance in micron-sized Si with a dislocation-scarce microstructure. A new analytical model was proposed to accurately evaluate the size effect in Si at different temperatures.

Supplementary data to this article can be found online at https://doi.org/10.1016/j.matdes.2020.108506.

CRediT authorship contribution statement

Ming Chen: Investigation, Writing - original draft, Writing - review & editing. **Juri Wehrs:** Investigation, Writing - review & editing. **Alla S. Sologubenko:** Investigation, Writing - review & editing. **Jacques Rabier:** Resources, Writing - review & editing. **Johann Michler:** Resources, Writing - review & editing. **Jeffrey M. Wheeler:** Conceptualization, Investigation, Supervision, Writing - review & editing.

Declaration of competing interest

The authors declare no competing financial interest.

Acknowledgements

M.C. and J.M.W. would like to thank C. Zaubitzer and K. Kunze (ScopeM, ETH Zurich) for their help in the sample preparation using FIB and HRSEM characterization. The authors thank R. Spolenak for his overall support of this work. We are grateful for the financial support of the Swiss National Science Foundation (SNSF Grant: 200021_166094).

References

[1] M.D. Uchic, D.M. Dimiduk, J.N. Florando, W.D. Nix, Sample dimensions influence strength and crystal plasticity, Science 305 (5686) (2004) 986–989.
[2] J. Rabier, L. Pizzagalli, J.L. Demenet, Chapter 93 Dislocations in Silicon at High Stress, 16, 2010 47–108.
[3] I. Yonenaga, An overview of plasticity of Si crystals governed by dislocation motion, Eng. Fract. Mech. 147 (2015) 468–479.
[4] J.P. Hirth, J. Lothe, Theory of Dislocations, 1982.
[5] J. Kim, D. Cho, R.S. Muller, Why Is (111) Silicon a Better Mechanical Material for MEMS?, Transducers' 01 Eurosensors XV, Springer, 2001 662–665.
[6] E. Aerts, P. Delavignette, R. Siems, S. Amelinckx, Stacking fault energy in silicon, J. Appl. Phys. 33 (10) (1962) 3078–3080.
[7] J. Rabier, P. Renault, D. Eyidi, J. Demenet, J. Chen, H. Couvy, L. Wang, Plastic deformation of silicon between 20 C and 425 C, Phys. Status Solidi C 4 (8) (2007) 3110–3114.
[8] J. Castaing, P. Veyssiere, L. Kubin, J. Rabier, The plastic deformation of silicon between 300 C and 600 C, Philosophical Magazine A 44 (6) (1981) 1407–1413.
[9] J. Michel, M. Omri, A. Oueldennaoua, A. George, Plastic deformation and surface investigation of ⟨100⟩ oriented silicon single crystals, Scr. Metall. 16 (6) (1982) 677–682.
[10] S. Pizzini, S. Binetti, A. Le Donne, A. Marzegalli, J. Rabier, Optical properties of shuffle dislocations in silicon, Appl. Phys. Lett. 88 (21) (2006), 211910.
[11] J.E. Bradby, J.S. Williams, M.V. Swain, In situ electrical characterization of phase transformations in Si during indentation, Phys. Rev. B 67 (8) (2003).
[12] A.M. Minor §, E.T. Lilleodden, M. Jin, E.A. Stach, D.C. Chrzan, J.W. Morris, Room temperature dislocation plasticity in silicon, Philos. Mag. 85(2–3) (2005) 323–330.
[13] S. Korte, J.S. Barnard, R.J. Stearn, W.J. Clegg, Deformation of silicon – insights from microcompression testing at 25–500°C, Int. J. Plast. 27 (11) (2011) 1853–1866.
[14] A. Merabet, M. Texier, C. Tromas, S. Brochard, L. Pizzagalli, L. Thilly, J. Rabier, A. Talneau, Y.M. Le Vaillant, O. Thomas, J. Godet, Low-temperature intrinsic plasticity in silicon at small scales, Acta Mater. 161 (2018) 54–60.
[15] F. Östlund, K. Rzepiejewska-Malyska, K. Leifer, L.M. Hale, Y. Tang, R. Ballarini, W.W. Gerberich, J. Michler, Brittle-to-ductile transition in uniaxial compression of silicon pillars at room temperature, Adv. Funct. Mater. 19 (15) (2009) 2439–2444.
[16] D. Kiener, C. Motz, M. Rester, M. Jenko, G. Dehm, FIB damage of Cu and possible consequences for miniaturized mechanical tests, Mater. Sci. Eng. A 459 (1) (2007) 262–272.
[17] Y. Wang, D. Xie, X. Ning, Z. Shan, Thermal treatment-induced ductile-to-brittle transition of submicron-sized Si pillars fabricated by focused ion beam, Appl. Phys. Lett. 106 (8) (2015) 81905.
[18] J.K. Bhardwaj, H. Ashraf, Advanced Silicon Etching Using High-density Plasmas, Micromachining and Microfabrication, International Society for Optics and Photonics, 1995 224–233.
[19] B. Moser, K. Wasmer, L. Barbieri, J. Michler, Strength and fracture of Si micropillars: a new scanning electron microscopy-based micro-compression test, J. Mater. Res. 22 (4) (2011) 1004–1011.
[20] H. Fei, A. Abraham, N. Chawla, H. Jiang, Evaluation of micro-pillar compression tests for accurate determination of elastic-plastic constitutive relations, J. Appl. Mech. 79 (6) (2012), 061011.
[21] J. Wheeler, J. Michler, Elevated temperature, nano-mechanical testing in situ in the scanning electron microscope, Rev. Sci. Instrum. 84 (4) (2013), 045103.
[22] S. Korte, W. Clegg, Micropillar compression of ceramics at elevated temperatures, Scr. Mater. 60 (9) (2009) 807–810.
[23] J. Wheeler, P. Brodard, J. Michler, Elevated temperature, in situ indentation with calibrated contact temperatures, Philos. Mag. 92 (25–27) (2012) 3128–3141.
[24] M. Chen, J. Wehrs, J. Michler, J.M. Wheeler, High-temperature in situ deformation of GaAs micro-pillars: lithography versus FIB machining, Jom 68 (11) (2016) 2761–2767.
[25] V. Maier, K. Durst, J. Mueller, B. Backes, H.W. Höppel, M. Göken, Nanoindentation strain-rate jump tests for determining the local strain-rate sensitivity in nanocrystalline Ni and ultrafine-grained Al, J. Mater. Res. 26 (11) (2011) 1421–1430.
[26] J.M. Wheeler, L. Thilly, A. Morel, A.A. Taylor, A. Montagne, R. Ghisleni, J. Michler, The plasticity of indium antimonide: insights from variable temperature, strain rate jump micro-compression testing, Acta Mater. 106 (2016) 283–289.
[27] G. Mohanty, J.M. Wheeler, R. Raghavan, J. Wehrs, M. Hasegawa, S. Mischler, L. Philippe, J. Michler, Elevated temperature, strain rate jump microcompression of nanocrystalline nickel, Philos. Mag. 95 (16–18) (2014) 1878–1895.
[28] D. Caillard, J.-L. Martin, Thermally Activated Mechanisms in Crystal Plasticity, Elsevier, 2003.
[29] B.N. Jaya, J.M. Wheeler, J. Wehrs, J.P. Best, R. Soler, J. Michler, C. Kirchlechner, G. Dehm, Microscale fracture behavior of single crystal silicon beams at elevated temperatures, Nano Lett. 16 (12) (2016) 7597–7603.
[30] C.M. Lauener, L. Petho, M. Chen, Y. Xiao, J. Michler, J.M. Wheeler, Fracture of silicon: influence of rate, positioning accuracy, FIB machining, and elevated temperatures on toughness measured by pillar indentation splitting, Mater. Des. 142 (2018) 340–349.
[31] G. Mohanty, J. Wehrs, B.L. Boyce, A. Taylor, M. Hasegawa, L. Philippe, J. Michler, Room temperature stress relaxation in nanocrystalline Ni measured by micropillar compression and miniature tension, J. Mater. Res. 31 (8) (2016) 1085–1095.
[32] J. Rabier, A. Montagne, J.M. Wheeler, J.L. Demenet, J. Michler, R. Ghisleni, Silicon micropillars: high stress plasticity, Phys. Status Solidi C 10 (1) (2013) 11–15.
[33] J. Demenet, J. Desoyer, J. Rabier, P. Veyssiere, On the plasticity of silicon below 650° C, Scr. Metall. 18 (1) (1984) 41–45.
[34] G.M. Pharr, E.G. Herbert, Y. Gao, The indentation size effect: a critical examination of experimental observations and mechanistic interpretations, Annu. Rev. Mater. Res. 40 (1) (2010) 271–292.
[35] T.A. Parthasarathy, S.I. Rao, D.M. Dimiduk, M.D. Uchic, D.R. Trinkle, Contribution to size effect of yield strength from the stochastics of dislocation source lengths in finite samples, Scr. Mater. 56 (4) (2007) 313–316.
[36] T. Suzuki, T. Yasutomi, T. Tokuoka, I. Yonenaga, Plasticity of III—V compounds at low temperatures, Phys. Status Solidi A 171 (1) (1999) 47–52.
[37] T.H. Courtney, Mechanical Behavior of Materials, Waveland Press, 2005.
[38] I. Yonenaga, K. Sumino, Dislocation dynamics in the plastic deformation of silicon crystals I. Experiments, Phys. Status Solidi A 50 (2) (1978) 685–693.
[39] N. Miyazaki, Y. Kuroda, Dislocation density simulations for bulk single crystal growth process, Met. Mater. 4 (4) (1998) 883–890.
[40] G. Schoeck, The activation energy of dislocation movement, Phys. Status Solidi B 8 (2) (1965) 499–507.
[41] F.R. Nabarro, M.S. Duesbery, Dislocations in Solids, Elsevier, 2002.
[42] J. Godet, J. Rabier, Propagation of stacking faults from "composite" dislocation cores at low temperature in silicon nanostructures, J. Phys. Conf. Ser. 1190 (2019) 12007.
[43] A.J. Wagner, E.D. Hintsala, P. Kumar, W.W. Gerberich, K.A. Mkhoyan, Mechanisms of plasticity in near-theoretical strength sub-100 nm Si nanocubes, Acta Mater. 100 (2015) 256–265.
[44] Q. Wei, H. Zhang, B. Schuster, K. Ramesh, R. Valiev, L. Kecskes, R. Dowding, L. Magness, K. Cho, Microstructure and mechanical properties of super-strong nanocrystalline tungsten processed by high-pressure torsion, Acta Mater. 54 (15) (2006) 4079–4089.
[45] D. Kiener, R. Fritz, M. Alfreider, A. Leitner, R. Pippan, V. Maier-Kiener, Rate limiting deformation mechanisms of bcc metals in confined volumes, Acta Mater. 166 (2019) 687–701.
[46] D. Hull, D.J. Bacon, Introduction to Dislocations, Butterworth-Heinemann, 2001.
[47] Y. Zou, J.M. Wheeler, H. Ma, P. Okle, R. Spolenak, Nanocrystalline high-entropy alloys: a new paradigm in high-temperature strength and stability, Nano Lett. 17 (3) (2017) 1569–1574.
[48] T. Zhu, J. Li, A. Samanta, A. Leach, K. Gall, Temperature and strain-rate dependence of surface dislocation nucleation, Phys. Rev. Lett. 100 (2) (2008), 025502.
[49] L. Pizzagalli, P. Beauchamp, First principles determination of the Peierls stress of the shuffle screw dislocation in silicon, Philos. Mag. Lett. 84 (11) (2004) 729–736.
[50] A. George, J. Rabier, Dislocations and plasticity in semiconductors. I — Dislocation structures and dynamics, Revue de Physique Appliquée 22 (9) (1987) 941–966.
[51] W. Blum, Discussion: activation volumes of plastic deformation of crystals, Scr. Mater. 146 (2018) 27–30.

[52] M.A. Hopcroft, W.D. Nix, T.W. Kenny, What is the Young's modulus of silicon? J. Microelectromech. Syst. 19 (2) (2010) 229–238.
[53] D. Roundy, M.L. Cohen, Ideal strength of diamond, Si, and Ge, Phys. Rev. B 64 (21) (2001).
[54] J.R. Greer, J.T.M. De Hosson, Plasticity in small-sized metallic systems: intrinsic versus extrinsic size effect, Prog. Mater. Sci. 56 (6) (2011) 654–724.
[55] F. Östlund, P.R. Howie, R. Ghisleni, S. Korte, K. Leifer, W.J. Clegg, J. Michler, Ductile–brittle transition in micropillar compression of GaAs at room temperature, Philos. Mag. 91 (7–9) (2011) 1190–1199.
[56] O. Torrents Abad, J.M. Wheeler, J. Michler, A.S. Schneider, E. Arzt, Temperature-dependent size effects on the strength of Ta and W micropillars, Acta Mater. 103 (2016) 483–494.
[57] M.J. Burek, J.R. Greer, Fabrication and microstructure control of nanoscale mechanical testing specimens via electron beam lithography and electroplating, Nano Lett. 10 (1) (2009) 69–76.
[58] S.-W. Lee, W.D. Nix, Size dependence of the yield strength of fcc and bcc metallic micropillars with diameters of a few micrometers, Philos. Mag. 92 (10) (2012) 1238–1260.
[59] J. Shin, L.Y. Chen, U.T. Sanli, G. Richter, S. Labat, M.-I. Richard, T. Cornelius, O. Thomas, D.S. Gianola, Controlling dislocation nucleation-mediated plasticity in nanostructures via surface modification, Acta Mater. 166 (2019) 572–586.
[60] Y. Liu, E. Van der Giessen, A. Needleman, An analysis of dislocation nucleation near a free surface, Int. J. Solids Struct. 44 (6) (2007) 1719–1732.
[61] Z. Liu, W. Skrotzki, Slip on {100} planes in LiF, Phys. Status Solidi A 70 (2) (1982) 433–440.
[62] S.I. Rao, D.M. Dimiduk, M. Tang, M.D. Uchic, T.A. Parthasarathy, C. Woodward, Estimating the strength of single-ended dislocation sources in micron-sized single crystals, Philos. Mag. 87 (30) (2007) 4777–4794.
[63] H. Bei, S. Shim, M. Miller, G. Pharr, E. George, Effects of focused ion beam milling on the nanomechanical behavior of a molybdenum-alloy single crystal, Appl. Phys. Lett. 91 (11) (2007), 111915.
[64] A.T. Jennings, C. Gross, F. Greer, Z.H. Aitken, S.W. Lee, C.R. Weinberger, J.R. Greer, Higher compressive strengths and the Bauschinger effect in conformally passivated copper nanopillars, Acta Mater. 60 (8) (2012) 3444–3455.
[65] M.B. Lowry, D. Kiener, M.M. LeBlanc, C. Chisholm, J.N. Florando, J.W. Morris, A.M. Minor, Achieving the ideal strength in annealed molybdenum nanopillars, Acta Mater. 58 (15) (2010) 5160–5167.
[66] H. Bei, S. Shim, G.M. Pharr, E.P. George, Effects of pre-strain on the compressive stress–strain response of Mo-alloy single-crystal micropillars, Acta Mater. 56 (17) (2008) 4762–4770.